

# Innovative Dextran-Silver Nanoparticle Hydrogel for Potential Antibacterial Protection in Clinical Application

Kanimozhi Jeyaram<sup>1,\*</sup> , Sivasubramanian Velmurugan<sup>2,\*</sup>, Aathimoolam Narayanan<sup>1</sup>, Sumathi Ramasamay<sup>1</sup>, Ethiraj Selvarajan<sup>3</sup>

<sup>1</sup> Department of Biotechnology, School of Bio, Chemical and Processing Engineering, Kalasalingam Academy of Research and Education, Tamil Nadu, India; [kanimozhi.j@klu.ac.in](mailto:kanimozhi.j@klu.ac.in) (K.J.); [r9923101002@klu.ac.in](mailto:r9923101002@klu.ac.in) (A.N.); [sumathi@klu.ac.in](mailto:sumathi@klu.ac.in) (S.R.);

<sup>2</sup> Department of Chemical Engineering, National Institute of Technology, Calicut, Kerala, India; [siva@nitc.ac.in](mailto:siva@nitc.ac.in);

<sup>3</sup> Department of Genetic Engineering, School of Bioengineering, Faculty of Engineering and Technology, SRM Institute of Science and Technology (SRM IST), Kattankulathur – 603203, Chengalpattu District, Tamil Nadu, India. ; [selvarae@srmist.edu.in](mailto:selvarae@srmist.edu.in);

\* Correspondence: [kanimozhi.j@klu.ac.in](mailto:kanimozhi.j@klu.ac.in) (K.J.); [siva@nitc.ac.in](mailto:siva@nitc.ac.in) (S.V.);

Received: 3.08.2024; Accepted: 5.11.2025; Published: 20.12.2025

**Abstract:** This study explores the synthesis, characterization, and antibacterial activity of silver nanoparticles (AgNPs) derived from dextran produced by *Weissella cibaria*. Dextran-capped AgNPs (DEX-AgNPs) and physically crosslinked hydrogel composites with polyvinyl alcohol (PVA) were prepared and characterized using UV-vis spectroscopy, FTIR, XRD, TGA, tensile strength analysis, SEM, and TEM with SAED. Antibacterial efficacy was evaluated against *Staphylococcus aureus*, and molecular docking and inhibition constant analyses were performed against the potential targets, staphyloferrin A and B. The synthesized DEX-AgNPs exhibited a spherical morphology with sizes ranging from 5 to 7 nm. The PVA/(DEX-AgNPs) hydrogel composite exhibited improved mechanical properties, thermal stability, and controlled AgNP distribution compared to DEX-PVA and DEX-AgNPs alone. The swollen hydrogel patch demonstrated enhanced antibacterial activity owing to the sustained release of the DEX-AgNPs. Molecular docking revealed a strong binding affinity of dextran with staphyloferrin A and B, suggesting the inhibition of iron acquisition pathways in *S. aureus*. The biodegradable nature of the PVA-dextran hydrogel, combined with the presence of AgNPs, is anticipated to effectively curb bacterial exudate production and enhance antibacterial activity. This study highlights the potential of the developed DEX-AgNP hydrogel composite as a promising nanomedicine for clinical wound-dressing applications, particularly for combating antibiotic-resistant *S. aureus* infection.

**Keywords:** Dextran; silver nanoparticles; antibacterial activity; hydrogel; *Staphylococcus aureus*; Staphyloferrin A; Staphyloferrin B.

© 2025 by the authors. This article is an open-access article distributed under the terms and conditions of the Creative Commons Attribution (CC BY) license (<https://creativecommons.org/licenses/by/4.0/>), which permits unrestricted use, distribution, and reproduction in any medium, provided the original work is properly cited. The authors retain copyright of their work, and no permission is required from the authors or the publisher to reuse or distribute this article, as long as proper attribution is given to the original source.

## 1. Introduction

Hydrogels, characterized by their three-dimensional polymeric and hydrophilic matrices, exhibit an exceptional ability to absorb significant volumes of water [1]. This remarkable property, which is essential for their application in wound dressing materials, is attributed to the diverse functional groups present in the polymer network, including amino, carboxyl, amide, hydroxyl, and sulfonic groups [2]. Typically, well-defined hydrogel structures

can be modified to achieve customizable functionality and release profiles, particularly for applications involving antibacterial properties [3]. They have been applied across diverse fields, including transdermal patches, drug-delivery devices, wound dressings, tissue-engineering scaffolds, and contact lenses [4]. In biomedical applications, swollen hydrogels are widely used as powerful biomaterials due to their soft, rubbery nature and their ability to induce minimal tissue irritation [5]. Hydrogels can be formulated using natural polymers, such as collagen, starch, hyaluronate, chitosan, alginate, and dextran, or synthetic polymers, such as polyvinyl alcohol (PVA), polyethylene glycol (PEG), and polyhydroxyethyl methacrylate (HPMA) [6]. Furthermore, most PVA hydrogels undergo physical crosslinking, thereby avoiding the drawbacks of chemical crosslinkers. Additionally, physically crosslinked PVA hydrogels are commonly preferred for applications such as tissue engineering and oral administration due to their key properties [7,8]. PVA hydrogels prepared by the freeze-thaw technique have emerged as a clear preference owing to their remarkable toughness, rubbery elasticity, non-toxicity, and ready acceptance by the body [9]. Previously, the cross-linking of the carbohydrate polymer dextran (a homopolysaccharide of glucose) with PVA was aimed at augmenting the structural components of the PVA matrix, resulting in a lamellar appearance and distinct preferential orientation within the matrix [1,10]. Moreover, dextran and its derivatives exhibit immunomodulatory and anticoagulant properties [11].

Nanoparticles measuring 1-100 nm have garnered significant attention across various scientific disciplines owing to their unique characteristics and potential applications across multiple industries [12]. In particular, metal nanoparticles, such as those made from gold, silver, zinc, and copper, are of interest for wound-dressing applications due to their antibacterial properties and their ability to promote tissue healing. Silver nanoparticles (AgNPs) have unique physicochemical properties and wide-ranging applications in various fields. These are highly effective antimicrobial agents [13]. Their ability to target a broad spectrum of bacteria, viruses, and fungi makes them suitable for use in wound dressings, medical device coating, and drug delivery systems [14,15]. Their contribution to enhancing antibiotic efficacy and the low likelihood of inducing resistance further highlights their potential in the biomedical field [16]. AgNPs have been synthesized using various chemical and physical methods [17]. AgNPs are typically created using reductants such as borohydride, citrate, polymeric materials, ascorbate, and other organic reagents in the presence of silver nitrate [18]. Polysaccharides are used in green methods to synthesize AgNPs, which show promise against bacterial infections and possess a range of medicinal properties [19]. Polysaccharides widely used in the production of silver nanoparticles (SNPs) include chitosan [20], dextran [21], pullulan [21], and sodium alginate [22]. They have been chemically cross-linked with AgNPs, comprising PVA and dextran, and are intended for use in wound dressing applications [23]. However, the stabilization of AgNPs, regulation of their shape and size, and their distribution within the hydrogel matrix impose constraints on achieving optimal antibacterial activity and water absorption potential against pathogens [24]. Moreover, hydrogel scaffolds composed of dextran are known for their ability to enhance angiogenic responses and facilitate comprehensive skin regeneration during the healing of burn wounds [25].

Furthermore, the capacity of the hydrogels was limited. Given the functional role of AgNP-incorporated dextran-PVA hydrogels in antibacterial activity, this study aimed to overcome their limitations. Consequently, the incorporation of AgNPs into a dextran-PVA

hydrogel has emerged as a promising approach for potent antibacterial activity under high exudate conditions.

This ongoing research is directed toward the development of a physically cross-linked PVA/(DEX-AgNP) hydrogel patch tailored for high-exudate pathogens. Hydrogels composed of PVA and bacterial polysaccharides are expected to be biodegradable and effectively curb antibacterial exudate production. Additionally, the presence of dextran and AgNPs likely enhanced the antibacterial activity.

## 2. Materials and Methods

### 2.1. Chemicals and Bacterial Strains.

Polyvinyl alcohol (PVA) was procured from Sigma-Aldrich, Karnataka (India), and silver nitrate and all additional chemicals were obtained from Merck India Private Ltd. *Weissella cibaria* NITCSK4 (GenBank accession number KX387868) produces dextran polymers exceeding 2000 kDa, which were used as nitrate-reducing agents. *S. aureus* strains were obtained from the National Collection of Industrial Microorganisms (Pune, India). Deionized water was used in all the experiments.

### 2.2. Synthesis of DEX-AgNPs.

Dextran, derived from *Weissella cibaria* NITCSK4, isolated from the Sugarcane Extract at the Chemical Engineering Department of the National Institute of Technology Calicut, Kerala, India [26], was used to synthesize DEX-AgNPs. Colloids were prepared according to a previously described method with slight modifications [27]. DEX-AgNPs were formed by mixing 0.01M silver nitrate with varying concentrations of dextran solution (1%, 2%, 5%, and 10%), and adding 0.001 M sodium hydroxide (NaOH). The solution was vigorously stirred at 50°C for 2 h, and the development of a dark yellowish-brown color indicated the successful formation of metallic dextran AgNPs (DEX-AgNPs).

### 2.3. Preparation of DEX-PVA hydrogel composite.

Aqueous solutions of dextran (5% and 10%) in a 1:2 ratio were thoroughly mixed and stirred at 50°C for 2 h. The hydrogel, denoted as Dextran and PVA (DEX-PVA), was subjected to the freeze-thaw technique, as outlined in [28]. The DEX-PVA solutions were mixed and then poured into 90 mm Petri dishes using a 1 mm-thick mold. After the solutions cooled to 30°C and any bubbles were removed, the clear solutions were poured into molds and subjected to 8 freeze-thaw cycles. The cycles involved freezing at -20°C for 8 h and thawing at 37 ± 2°C for 5 h. The resulting gel was thoroughly washed with distilled water to remove unbound dextran and PVA residues. The films and gels were dehydrated in a desiccator at 37°C for several weeks. This cyclic process facilitated the crosslinking of DEX-PVA and hydrogel formation..

### 2.4. Preparation of PVA/(DEX-AgNPs) hydrogel composite.

A solution containing 10% PVA and DEX-AgNPs was thoroughly mixed and stirred at 50°C for 2 h. The hydrogel, denoted PVA/(DEX-AgNPs), was prepared using the freeze-thaw

technique as previously described [29]. The prepared hydrogel was then dried and transformed into a film for further analysis.

### 2.5. UV–vis spectrophotometer

UV–visible spectra of Dextran, DEX-PVA, DEX-AgNPs, and PVA/(DEX-AgNPs) were obtained using a UV-vis spectrophotometer (Perkin-Elmer UV Win Lab 6.2.0.0741/1.61.00 Lambda 650) within a wavelength range of 200 nm to 800 nm.

### 2.6. Fourier-transform infrared (FTIR) spectroscopy.

Fourier Transform Infrared (FTIR) spectroscopy analysis was conducted on Dextran, DEX-PVA, DEX-AgNPs, and PVA/(DEX-AgNPs) using an FTIR spectroscopy (Agilent Carry630 1B Diamond ATR module) over the wavelength range of 400-4000  $\text{cm}^{-1}$ .

### 2.7. X-ray diffractometer (XRD).

The structural properties of the dried DEX-PVA, PVA/(DEX-AgNP), and PVA/(DEX-AgNPs) hydrogels were determined by X-ray diffraction (XRD) using a Rigaku Miniflex 600 diffractometer. The scans were performed over  $3-90^\circ 2\theta$  (Cu- $K\alpha$  as the X-ray source), and the XRD patterns of all samples were recorded using a sodium iodide (NaI) scintillation detector with a graphite monochromator.

### 2.8. Swelling ratio.

The swelling properties of the hydrogels were assessed by determining the swelling indices. Initially, a pre-weighed small piece of dried hydrogel was introduced into a 50 mL vial, followed by the addition of 10 mL of Millipore water as the release medium. The vials were maintained under static conditions at  $35^\circ\text{C}$  for 12 h. As a characteristic of swelling, the mesh size of the swollen gel increased, enabling determination of the swelling index [30]. The equilibrium swelling ratio (SR) of the hydrogels was calculated using Equation (1).  $SR =$

$$\left[ \frac{W_s - W_d}{W_d} \times 100 \right] \quad (1)$$

Where  $W_s$  represents the weight of the swollen hydrogel, and  $W_d$  indicates the dry weight of the hydrogel.

### 2.9. Thermogravimetric analysis.

The mechanical stabilities of the hydrogel films, including PVA (conventional film), DEX-PVA, and (PVA/(DEX-AgNPs)), were assessed through tensile strength analysis. The hydrogel films were cut into dumbbell shapes for analysis, which was conducted using a Shimadzu universal testing machine (Autograph AG-S plus 10kN) at a crosshead speed of 10 mm/min at room temperature. Four measurements were performed for each sample to ensure reproducibility of the results. The thermostabilities of dextran, PVA, DEX-PVA, and PVA/(DEX-AgNPs) were evaluated using thermogravimetric analysis (TGA). Non-isothermal experiments were performed using a TGA STA7200 (SOFTWARE TA7000) module coupled with a thermal analyzer. The heating rate was set at  $10^\circ\text{C}/\text{min}$  in the temperature range of  $32-800^\circ\text{C}$  under a nitrogen atmosphere to obtain the TGA curves.

### 2.10. Scanning electron microscopy.

Electron micrographs of DEX-PVA, DEX-AgNPs, and PVA/(DEX-AgNPs) were captured using a Hitachi SU6600 Scanning Electron Microscope (SEM). A fragment of the film/gel mat was affixed to conductive carbon tape, mounted on the support, and subsequently coated with an approximately 6-nanometer layer of gold (Au) for 60 s.

### 2.11. Transmission electron microscopy (TEM).

The particle sizes of DEX-AgNPs and PVA/(DEX-AgNPs) were examined using a Transmission Electron Microscope (TEM) (Jeol/JEM 2100) operating at an accelerating voltage of 200 kV. A drop of the aqueous AgNPs solution was directly deposited onto a carbon-coated copper grid and allowed to air-dry thoroughly before TEM observations.

### 2.12. In vitro assessment of antibacterial activity.

The antibacterial activities of dextran, DEX-AgNPs, and PVA/(DEX-AgNPs) were assessed using the agar well diffusion method [31,32]. The analysis included testing for *Staphylococcus aureus*. A 0.85% physiological saline solution served as the negative control. The antibacterial activities of the prepared Dextran, DEX-AgNPs, and PVA/(DEX-AgNPs), and film materials were compared on a Muller-Hinton agar plate. All plates were incubated at 37°C for 24 h. Following incubation, bacterial activity, zone of inhibition, and statistical significance were observed.

### 2.13. Molecular docking.

The interaction between dextran and the target protein was studied using molecular docking analysis. The selection of receptors was based on previous studies, and they play a significant role in extracting iron from the host of *S. aureus* [33]. Protein structures were retrieved from the Protein Data Bank (PDB ID: 2MLM, 7CBB, 4M54, 3WF, and 3LHS), which provides access to the 3D atomic coordinates. The protein structures were prepared for docking by removing the ligands and water, followed by the addition of polar hydrogen and Kollman's charges. Dextran was obtained from PubChem (ID: 4125253). AutoDock Vina (PyRx v0.8) was used for the docking analysis. The inhibitors were docked into the appropriate binding sites with a modified complex grid size of 80 × 60 × 50 Å. The complexes were run and saved in pdbqt format, and each complex was analyzed using Schrodinger Maestro 14.0. The 3D and 2D structures of the protein-ligand complexes were visualized using Maestro 14.0. The docking results were interpreted based on the binding sites and inhibition constants.

### 2.14. Inhibition constant analysis.

The inhibition rate of dextran targeting specific proteins was determined by assessing their binding affinity. The inhibition constant ( $K_i$ ) represents the strength of the bond between the inhibitor and protein [34]. It is calculated by considering the Gibbs free energy change ( $\Delta G$ ) associated with binding, the ideal gas constant ( $R$ ), which is equal to 8.314 J/mol·K, and the absolute temperature ( $T$ ) in Kelvin. The dextran inhibition constant was determined using Equation (2), as follows:

$$K_i = e^{\left(\frac{\Delta G}{RT}\right)} \quad (2)$$

### 2.15. Statistical analysis.

All experiments were performed independently in triplicate, and the data are expressed as the mean  $\pm$  standard deviation. A value of  $p < 0.05$ , calculated using SPSS v27 ANOVA with Post Hoc Tests, was considered significant. Graphs were plotted using OriginPro v2022.

## 3. Results and Discussion

### 3.1. Synthesis of DEX-AgNPs, hydrogel composite, and UV-visual spectrophotometer.

In this study, dextran-integrated AgNPs were synthesized via an *in situ* reduction process. Different dextran concentrations were used to prepare AgNPs. Initially, the colorless and transparent hydrogels became deep yellow, as shown in Figure 1 (a). The size and shape of the DEX-AgNPs were intricately linked to the concentrations of the metal precursor and reducing agent.

The effect of dextran concentration on the size distribution of AgNPs was investigated using UV-Vis spectral responses attributed to Surface Plasmon Resonance (SPR). Figure 1 (b) illustrates the size distribution of the AgNPs with varying dextran concentrations and their UV-Vis spectral responses. The DEX-AgNP solution exhibited radiation absorption in the visible range at 420 nm (Figure 1 (c)), confirming the presence of AgNPs via a strong SPR transition. As the dextran concentration increased, the peak half-width decreased, and the peak intensity increased, indicating a narrower distribution of Ag nanoparticles in dextran solutions with higher concentrations. Notably, Figure 1(a) and (b) show that the DEX-AgNPs prepared with a 10% dextran solution displayed enhanced absorption intensity, and the absorption peak shifted to a lower wavelength. This study demonstrates the effective *in situ* synthesis of dextran-stabilized silver nanoparticles (DEX-AgNPs) by varying dextran levels, yielding hydrogel composites with customizable optical and structural properties. The shift from clear hydrogels to a rich yellow hue (Figure 1a) serves as a visual indication of AgNP formation, which is attributed to surface plasmon resonance (SPR) effects [35].

The size and shape distributions of the PVA/(DEX-AgNPs) and DEX-AgNPs hydrogel composites can be used to explain the different absorbance peaks at 435 nm observed for Dextran and DEX-PVA. The UV-visible spectra are shown in Figures 1 (c) and (d) to illustrate the effect of dextran concentration on the size and size distribution of PVA/(DEX-AgNPs) and DEX-AgNPs, respectively. When PVA was added, a large number of DEX-AgNPs spread throughout the hydrogel network using all the reducing groups. The synthesis of DEX-AgNPs within the hydrogel was altered by increasing the concentration, leading to observable variations in the UV-Vis spectra of PVA/(DEX-AgNPs). The effects of hydrogels, including a cross-linking agent, on the shape and size distribution of PVA/(DEX-AgNPs) are shown in Figures S1 (a–f). Owing to the surface plasmon resonance effect, the typical absorption peak shifted from 435 nm to 420 nm for AgNPs in each hydrogel sample. Notably, the strongest signal at 435 nm was observed in both the presence and absence of PVA, suggesting the presence of DEX-AgNP clusters or nanoparticle aggregation. This clearly illustrates the distinct appearance of the hydrogel and the hydrogel with embedded Ag nanoparticles. The network formation around the DEX-AgNPs is illustrated in Figures S1 (a–f) and exhibited a clustered arrangement. This technique improves the effectiveness of dextran, and its films are shown in Figures 2 (a) and (b). The size and shape of AgNPs are significantly influenced by the concentrations of the metal precursor ( $\text{AgNO}_3$ ) and the reducing/stabilizing agent (dextran).

UV–Vis spectroscopy revealed the plasmonic properties of AgNPs synthesized at varying dextran concentrations (Figure 1c). The absorption peak was observed at approximately 420 nm. This is indicative of spherical AgNPs [36], and the narrowing of the SPR peak (i.e., a decrease in full-width at half-maximum) at elevated dextran concentrations suggests improved control over the particle size and reduced polydispersity. This is likely attributable to the increased presence of hydroxyl groups in dextran, which serve as both reducing and capping agents, thereby regulating the nucleation and growth of AgNPs [37]. Notably, a blue shift in the SPR peak (from 435 to 420 nm) was observed at higher dextran concentrations, indicating the formation of smaller nanoparticles in more concentrated dextran environments (Figures 1b–c). This observation is consistent with previous studies, which found that increasing stabilizer concentration led to finer nanoparticles due to accelerated reduction and enhanced surface passivation.

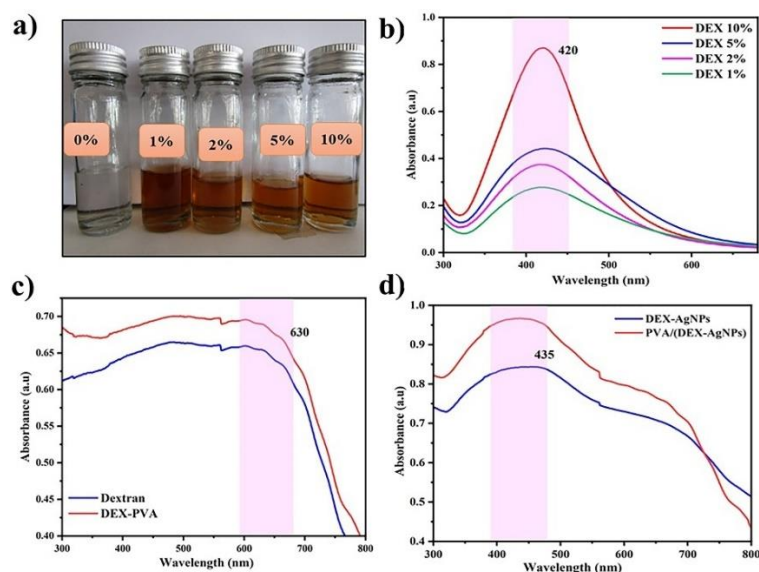


**Figure 1.** (a) Synthesis of Dextran-Silver nanoparticle (DEX-AgNP) at various concentrations of dextran; (b) UV-visible spectra of dextran-capped silver nanoparticle solution prepared at various concentrations of dextran (w/v). DEX-concentration of dextran ranges from 01 to 10% (w/v); (c) UV-visual spectra of Dextran and DEX-PVA; (d) DEX-AgNPs and PVA/(DEX-AgNPs).

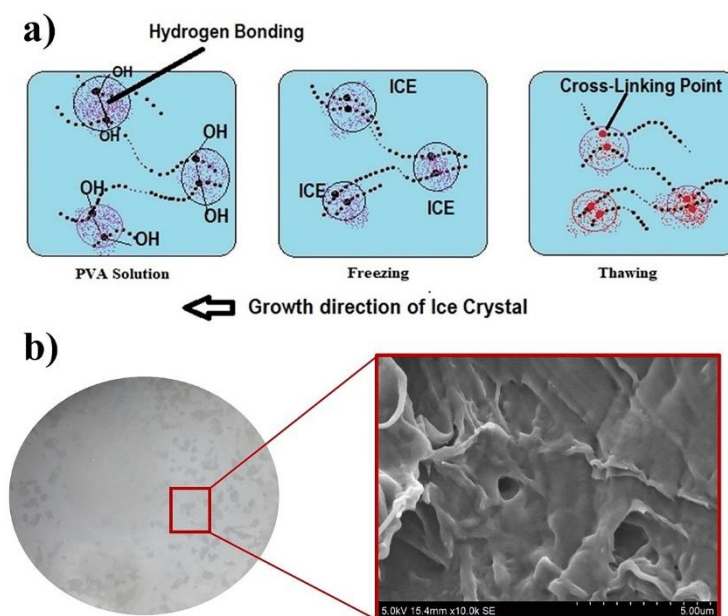


**Figure 2.** (a) Formation and cross-linking patterns of DEX-PVA and PVA/(DEX-AgNPs); (b) Dried hydrogel of DEX-PVA. SEM images refer to a matrix-like structure.

### 3.2. Fourier transform infrared spectrophotometer.

To investigate the molecular interactions and functional group participation in AgNPs synthesis and hydrogel formation, FTIR spectra of Dextran, DEX-PVA, DEX-AgNPs, and PVA/(DEX-AgNPs) were recorded, and are shown in Figure 3(a) and 3(b). The FTIR spectrum of dextran (Figure 3a) exhibits a broad peak at  $3265\text{ cm}^{-1}$ , corresponding to O–H stretching vibrations, indicative of strong intermolecular hydrogen bonding typical of polysaccharides. The band at  $2940\text{ cm}^{-1}$  is due to C–H stretching of aliphatic –CH groups. Further bands appear at  $1654\text{ cm}^{-1}$  (likely associated with absorbed water or C=O stretching from aldehydes or ketones), and a prominent peak at  $1084\text{ cm}^{-1}$ , attributed to C–O stretching vibrations of primary alcohols in dextran. The peaks at  $834\text{ cm}^{-1}$  correspond to the skeletal vibrations of the sugar rings, confirming the polysaccharide structure. Upon blending dextran with PVA (DEX-PVA), all the major bands remained, but some intensity enhancements and minor shifts were observed. Notably, the C–O stretching ( $1084\text{ cm}^{-1}$ ) and skeletal region ( $\sim 834\text{ cm}^{-1}$ ) become more defined, reflecting intermolecular hydrogen bonding between hydroxyl groups of PVA and dextran, consistent with earlier findings [38,39].

The FTIR spectrum of DEX-AgNPs (Figure 3b) closely resembled that of DEX-PVA, but with distinct spectral changes indicating nanoparticle formation. The intensity of the O–H peak ( $3265\text{ cm}^{-1}$ ) was slightly diminished, suggesting the involvement of hydroxyl groups in the bioreduction of  $\text{Ag}^+$  ions. The C–H bending peak shifted slightly to  $1412\text{ cm}^{-1}$ , and the skeletal vibrations remained, but with a modified intensity, implying conformational changes in the backbone. In the PVA/(DEX-AgNPs) composite hydrogel spectrum, O–H and C–H peaks ( $3265\text{ cm}^{-1}$  and  $2940\text{ cm}^{-1}$ ) are retained, but the peaks in the fingerprint region show major shifts and intensity alterations. The C–O peak remains near  $1084\text{ cm}^{-1}$ , but with reduced intensity. A new peak appears at  $670\text{ cm}^{-1}$ , possibly indicating Ag–O bond vibrations or lattice bending of the embedded AgNPs [40,41]. The reduction in the intensity of the  $1654\text{ cm}^{-1}$  band suggests that C=O groups also contributed to nanoparticle stabilization or hydrogel crosslinking.

The Comparative FTIR spectra confirmed that the hydroxyl, carboxyl, and nitrate-related groups in dextran and PVA were directly involved in both silver ion reduction and nanoparticle stabilization. Shifts in peaks and intensity changes in the  $1400\text{--}700\text{ cm}^{-1}$  region indicate the formation of Ag–O and possibly Ag–C or Ag–OH interactions, confirming the successful embedding of AgNPs in the hydrogel matrix.

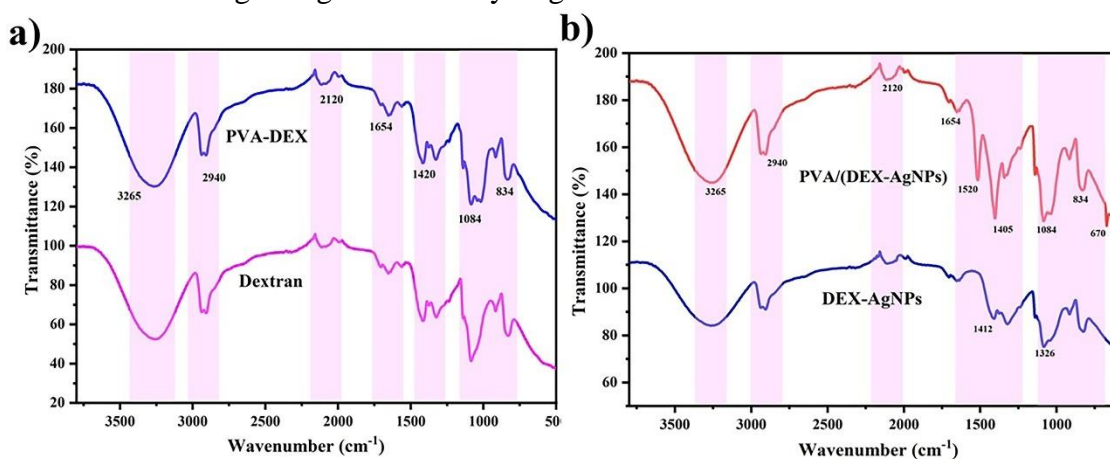


**Figure 3.** (a) FTIR spectrum of Dextran and DEX-PVA; (b) DEX-AgNPs and PVA/(DEX-AgNPs).

The observed hydrogen bonding and spectral shifts further support the formation of a stable polymeric network, which is consistent with previously reported bio-based AgNP systems [42,43].

### 3.4. X-ray diffraction.

Elemental confirmation and structural elucidation of DEX-AgNPs, DEX-PVA, and PVA/(DEX-AgNPs) hydrogels were performed using X-ray diffraction (XRD) analysis. The XRD patterns presented in Figure 4 (a–c) provide insights into the crystallinity and phase composition of the synthesized materials. The DEX-PVA composite exhibited distinct Bragg diffraction peaks at  $8.74^\circ$ ,  $29.28^\circ$ ,  $34.66^\circ$ ,  $56.52^\circ$ , and  $62.02^\circ$ , indicating semicrystalline domains within the polymer matrix. Similarly, the synthesized DEX-AgNPs displayed multiple sharp peaks at  $13.4^\circ$ ,  $16.88^\circ$ ,  $22.02^\circ$ ,  $32.2^\circ$ ,  $34.86^\circ$ ,  $36.66^\circ$ ,  $47.86^\circ$ ,  $56.92^\circ$ ,  $62.02^\circ$ ,  $68.2^\circ$ , and  $77.12^\circ$ , confirming the formation of AgNPs within the dextran matrix. These reflections are in good agreement with previously reported diffraction patterns for AgNPs synthesized using polysaccharides [44]. XRD analysis provides compelling evidence for the structural integrity and successful synthesis of the PVA/(DEX-AgNPs) hydrogel system. The distinct Bragg peaks observed in the individual components (DEX-PVA and DEX-AgNPs) and their retention in the composite confirmed that no phase degradation or disruption occurred during hydrogel formation. The presence of sharp, well-defined peaks in the DEX-AgNPs sample indicates the crystalline nature of the embedded silver nanoparticles, aligned with the face-centered cubic (FCC) structure of metallic silver, as noted in previous studies [44,45]. The XRD profile of the PVA/(DEX-AgNPs) hydrogel composite revealed characteristic peaks at  $8.66^\circ$ ,  $13.56^\circ$ ,  $17.06^\circ$ ,  $21.76^\circ$ ,  $25.76^\circ$ ,  $32.06^\circ$ ,  $34.78^\circ$ ,  $36.60^\circ$ ,  $44.14^\circ$ ,  $48.0^\circ$ ,  $57.1^\circ$ , and  $63.56^\circ$ , representing the combined crystalline contributions of PVA, dextran, and Ag silver nanoparticles, respectively. The presence of overlapping peaks in both individual and composite samples confirms the successful integration of all components and the formation of a multiphase hydrogel nanocomposite. These findings are corroborated by the similar XRD profiles reported for AgNP-loaded biopolymer systems [46,47].

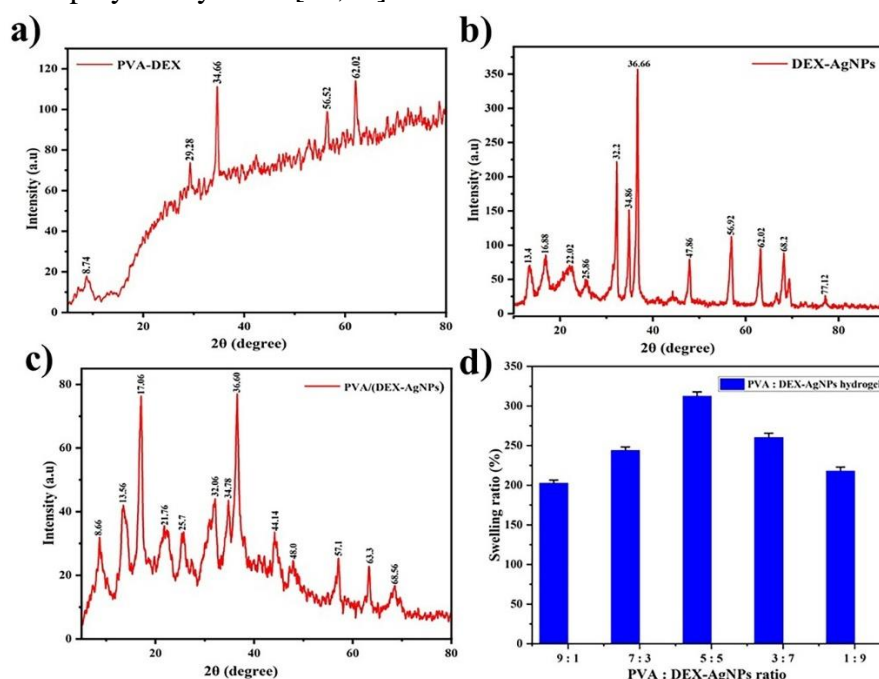


**Figure 4.** (a) X-ray diffraction pattern of PVA-DEX; (b) DEX-AgNPs; (c) PVA/(DEX-AgNPs); (d) Swelling Index of PVA: DEX-AgNPs.

In the composite hydrogel, the overlapping diffraction peaks from dextran and PVA suggest the formation of a semicrystalline network, which may influence the mechanical strength and swelling properties of the hydrogel. Furthermore, the retained crystallinity of the AgNPs within the hydrogel matrix suggests that the nanoparticles' antimicrobial efficacy and stability are preserved, an essential requirement for biomedical applications [48,49].

### 3.5. Swelling index.

The prepared DEX-AgNPs were cross-linked with PVA using the freeze–thaw method at various PVA-to-DEX-AgNP volume ratios: 9:1, 7:3, 5:5, 3:7, and 1:9. The effects of these concentrations on hydrogel rigidity were evaluated manually. After gel formation, the samples were desiccated, and the swelling index was calculated according to established procedures [50]. As shown in Figure 4(d), the visual images of the dried PVA/(DEX-AgNPs) hydrogel composites reveal distinct morphologies. The corresponding swelling indices are 2.03, 2.44, 3.13, 2.60, and 2.18, respectively. Notably, the hydrogel formed at the 5:5 ratio displayed the highest swelling index, suggesting an optimal network structure with enhanced water uptake. Upon water immersion, the dried hydrogel films exhibited significant expansion. This behavior was attributed to the hydrophilic nature of dextran, a biopolymer known for its high water-holding capacity and ability to form hydrogen bonds with water molecules [50,51]. The swelling facilitated the passive and sustained release of DEX-AgNPs from the hydrogel matrix under static aqueous conditions, without requiring an external retrieval process. These swelling-controlled release systems are valuable for biomedical and antimicrobial applications [52].

### 3.6. Tensile analysis and thermogravimetric analysis.

The percentage elongation and elastic modulus of PVA, DEX-PVA, and PVA/(DEX-AgNPs) hydrogel films are presented in Table 1. The mechanical and thermal properties of the synthesized PVA-based hydrogel films revealed the effects of dextran and silver nanoparticles (AgNPs) on the physicochemical characteristics of polyvinyl alcohol (PVA). The addition of dextran (DEX) and DEX-functionalized AgNPs significantly increased the tensile strength of pure PVA films, indicating effective crosslinking and reinforcement of the polymer matrix. The PVA/(DEX-AgNPs) hydrogel exhibited the greatest elongation at break (158.36%), indicating enhanced flexibility, while also achieving better tensile strength (34.708 N/mm<sup>2</sup>) compared to pure PVA (29.323 N/mm<sup>2</sup>). This improvement is likely due to the interaction between the hydroxyl groups of PVA and the DEX-AgNPs, resulting in a stronger, more elastic network. The elastic modulus results further confirmed the structural changes caused by the additives. The DEX-PVA hydrogel exhibited a higher Young's modulus (0.256 N/mm<sup>2</sup>) than both pure PVA (0.199 N/mm<sup>2</sup>) and PVA/(DEX-AgNPs) (0.221 N/mm<sup>2</sup>), indicating that dextran significantly contributes to network rigidity. Although the AgNPs-loaded hydrogel had a similar tensile strength, its slightly lower modulus might be attributed to the plasticizing effect of AgNPs or to agglomeration, which disrupts the uniform polymer packing [53].

**Table 1.** Tensile strength of PVA, PVA-DEX, and PVA/(DEX-AgNPs) hydrogel composite.

Materials	Elongation (%)	Tensile strength (N/mm <sup>2</sup> )	Young's modulus (N/mm <sup>2</sup> )
PVA	147.69	29.323	0.199
DEX-PVA	152.00	34.580	0.256
PVA/(DEX-AgNPs)	158.36	34.708	0.221

The thermal stability results presented in Figure 5 demonstrate that the DEX-PVA hydrogel film exhibited a higher thermal stability than the PVA/(DEX-AgNPs) hydrogel film. Thermal analysis showed that DEX-PVA films had the highest thermal degradation temperature ( $T_d = 340^\circ\text{C}$ ), followed by PVA/(DEX-AgNPs) ( $320^\circ\text{C}$ ), and pure PVA ( $300^\circ\text{C}$ ). This enhancement in thermal stability aligns with the literature, suggesting that dextran improves PVA's thermal stability through hydrogen bonding and intermolecular interactions [54]. However, the slightly lower  $T_d$  of the AgNPs-containing films could be due to the catalytic behavior of AgNPs, which has been shown to promote thermal degradation at lower temperatures [55]. Overall, the synergistic interaction among PVA, dextran, and AgNPs enhanced mechanical strength, elasticity, and thermal stability, making them suitable for biomedical and packaging applications. Moreover, the presence of AgNPs provides antimicrobial properties, further expanding their application potential in wound dressings, food preservation, and controlled drug release systems [55]. As shown in Table 1, the degradation temperature ( $T_d$ ) of the PVA/(DEX-AgNPs) hydrogel film is  $320^\circ\text{C}$ , which is lower than the  $340^\circ\text{C}$  observed for the DEX-PVA film. This suggests a reduction in thermal stability when AgNPs were added. Although silver nanoparticles are recognized for their antimicrobial and strengthening effects, they can negatively impact the thermal properties of polymer matrices. The reduced thermal stability of PVA/(DEX-AgNPs) hydrogels can be attributed to the catalytic properties of AgNPs, which facilitate oxidative or pyrolytic degradation reactions. As Lewis acid catalysts, silver nanoparticles can accelerate the breakdown of polymer chains at high temperatures, leading to chain scission and radical formation during thermal decomposition [56].

Furthermore, AgNPs might disrupt the hydrogen-bonding network in the PVA-dextran matrix, thereby decreasing crystallinity and weakening intermolecular forces. This disruption reduces the energy required for thermal degradation of the polymer [57]. The quality of AgNP dispersion within the matrix is also crucial; inadequate distribution or nanoparticle clumping can create localized defects or hot spots, which may trigger early thermal decomposition [58].

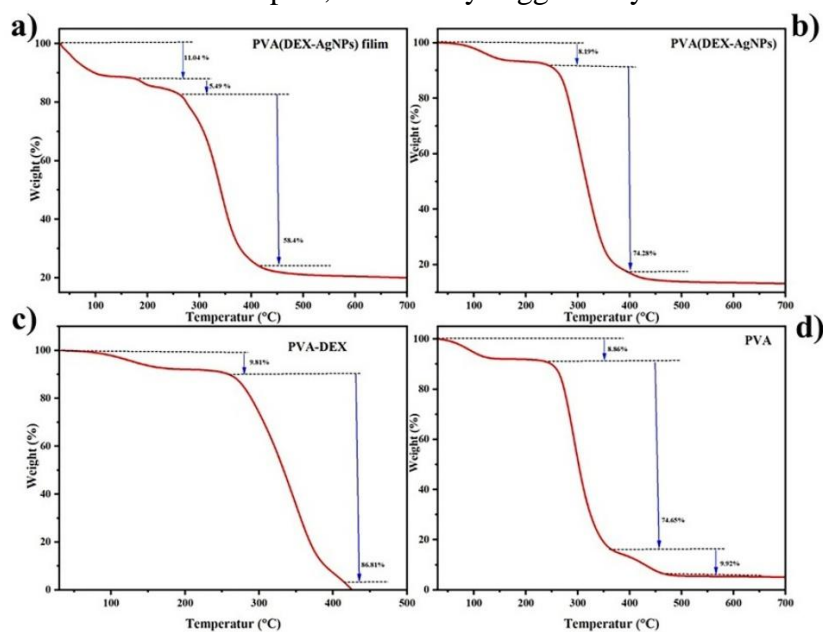


**Figure 5.** Thermogravimetric analysis of (a) PVA/(DEX-AgNPs) film, (b) PVA/(DEX-AgNPs), (c) PVA-DEX and (d) PVA

### 3.7. Scanning electron microscopy.

Scanning electron microscopy (SEM) was used to evaluate the surface structure and nanoparticle distribution in the synthesized hydrogels and composites. Figure 6a-e illustrates the DEX-PVA matrix, revealing a coarse fibrous texture with lamellar sheets and noticeable clusters of unreacted dextran (highlighted with yellow circles and red arrows). The incomplete integration of dextran within the PVA matrix led to phase separation, suggesting weak physical interactions or inadequate crosslinking under the synthesis conditions. This morphology indicates a heterogeneous structure, which potentially diminishes the mechanical strength and uniformity of the encapsulated nanoparticles. The SEM image in Figure 6b shows dense spherical nanoparticle aggregates within a dextran matrix. The relatively consistent cluster size confirmed the successful reduction of  $\text{Ag}^+$  ions by dextran, resulting in the formation of AgNPs. However, the limited stabilization capability of dextran alone likely contributes to particle aggregation, as observed in similar carbohydrate-based nanoparticle systems [59]. The absence of steric or electrostatic stabilization beyond the dextran coating may have facilitated the formation of clusters. The composite hydrogel depicted in Figure 6c exhibited a more compact, porous morphology with embedded nanoparticle clusters approximately 50 nm in size. The smoother surface and interconnected porous structure suggest improved cross-linking between PVA and the DEX-AgNPs, facilitating enhanced nanoparticle immobilization. The hydrogel matrix likely acts as a scaffold, minimizing aggregation and enabling controlled spatial distribution, as supported by studies of PVA-based nanocomposites [60]. At a higher magnification, Figures 6(d-e) provide detailed views of the nanoparticle morphology and size distribution. In Figure 6d (DEX-AgNPs), spherical AgNPs range from 19.39 nm to 74.90 nm, with evident aggregation. This wide size variation suggests that, although dextran acts as a reducing agent, its capacity to prevent nanoparticle coalescence is limited.

In contrast, Figure 6e (PVA/(DEX-AgNPs)) shows more uniform and smaller nanoparticles, ranging from 19.53 nm to 43.27 nm, evenly dispersed in the matrix. This confirms that incorporating PVA not only supports mechanical integrity but also contributes to the stabilization and size control of AgNPs. PVA contains multiple hydroxyl groups that are likely to coordinate with AgNPs and dextran, forming a semi-interpenetrating network that restricts nanoparticle mobility and aggregation [61].

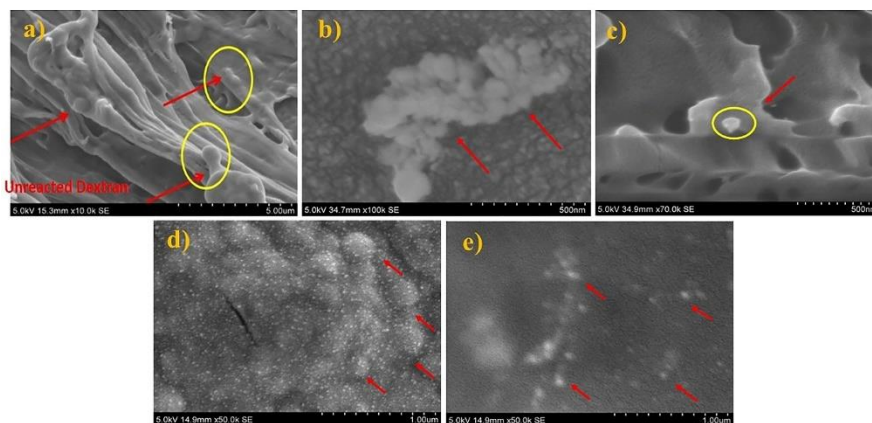


**Figure 6.** SEM micrographs of synthesized Dextran form (a) DEX-PVA;(b&c) DEX-AgNPs; (d&e)PVA/(DEX-AgNPs).

The morphological differences among the three systems (DEX-PVA, DEX-AgNPs, and PVA/(DEX-AgNPs)) highlight the synergistic roles of dextran and PVA in nanoparticle synthesis and stabilization. Although dextran facilitates the bio-reduction of silver ions, it lacks

sufficient steric hindrance to prevent aggregation. The addition of PVA introduced hydrogen bonding and crosslinking, enhancing nanoparticle dispersion and reducing size variability. These findings align with previous reports showing that polysaccharide-assisted AgNPs synthesis yielded effective reduction but required secondary polymers such as PVA or chitosan to achieve uniform stabilization and biomedical functionality [62,63]. The smaller and more homogeneously distributed AgNPs observed in the PVA/(DEX-AgNPs) composite are particularly advantageous for biomedical applications, such as antimicrobial hydrogels, wound dressings, and drug delivery systems.

### 3.8. Transmission electron microscope.

The size and shape of the synthesized DEX-AgNPs and the PVA/(DEX-AgNPs) hydrogel composite were determined. The synthesized dark-brown colloids were dried onto a carbon-coated 200-mesh copper grid for TEM examination. Figure 7 (a-f) present the TEM images of DEX-AgNPs and the PVA/(DEX-AgNPs) hydrogel composite, with the size distribution shown in Figure 7. (a, c, e, and f) Typical TEM images are depicted in Figure 7 (c & f), indicating that TEM analysis (Figure 7) verifies that both DEX-AgNPs and the PVA/(DEX-AgNPs) composites formed small, well-defined spherical nanoparticles, averaging 5–7 nm and 6–8 nm, respectively. This finding is consistent with those of earlier studies on dextran-mediated AgNPs synthesis. For instance, Carré-Rangel et al. demonstrated that dextran functions as both a reducing and stabilizing agent, producing nearly spherical AgNPs in the 1–10 nm range [64]. Our results highlight the role of polysaccharide matrices in limiting nanoparticle growth. Similar sizes (<10 nm) have been reported for dextran-capped AgNPs, supported by TEM images showing spheres between 5 and 8 nm[65]. The polymer network provides a confined environment that restricts aggregation and allows controlled nucleation, resulting in a narrow size distribution.

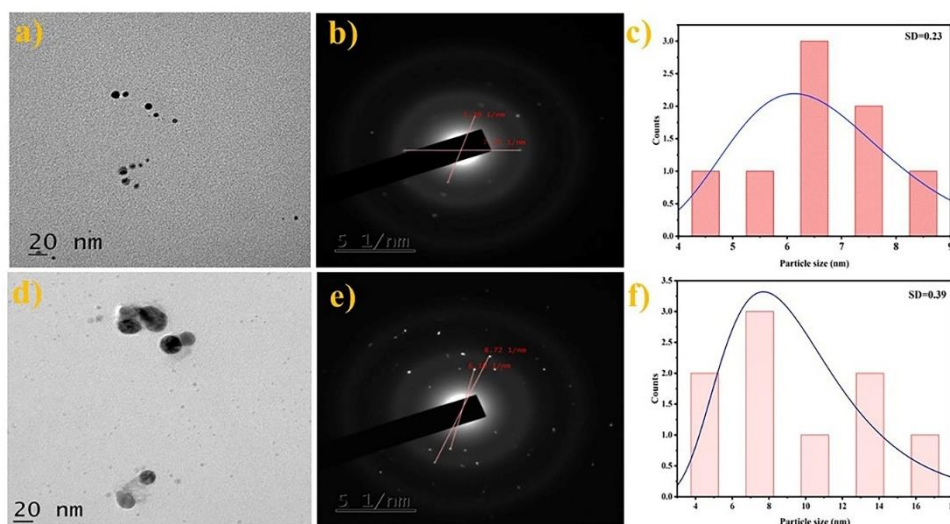


**Figure 7.** TEM micrographs of synthesized Dextran form (a, b, c) DEX-AgNPs; (d, e, f) PVA/(DEX-AgNPs).

### 3.9. In vitro assessment of antibacterial activity.

The agar well diffusion method was used to assess the biological activity of dextran against *Staphylococcus aureus*. DEX-PVA, DEX-AgNPs, and PVA/(DEX-AgNPs) demonstrated inhibition zones against bacteria, as illustrated in Tab 2. These results underscore the functional role of dextran from *Weissella cibaria* (NITCSK4) in clinical

applications. The study revealed that the hydrogel composite of swollen PVA crosslinked with dextran and AgNPs exhibited an enhanced inhibition zone compared to DEX-PVA and DEX-AgNPs. This remarkable improvement can be attributed to the release of the DEX-AgNPs from the swollen gel. The substantial diameter of the zone of inhibition observed for PVA/(DEX-AgNPs) suggested its potential use against pathogens. Furthermore, dextran exerts immunomodulatory effects [32]. Moreover, DEX-PVA, DEX-AgNPs, and PVA/(DEX-AgNPs) in the dried film of the hydrogel composite form displayed enlarged sizes after 24 h of inhibition, indicating a significant impact on the bacterial colonies. Hydrogels have a high water-holding capacity and can bind hydrogen molecules, which are crucial for bacterial colony formation, thereby contributing to their superior antibacterial activity. The DEX-AgNPs retrieved from the swollen gel also exhibited better activity than that of the PVA/(DEX-AgNPs) solution, as shown in Table 2. This difference could be attributed to the size of the AgNPs, a conclusion supported by the *in silico* results of the present study. The zone of inhibition was highest ( $28.33 \pm 0.5^c$ ) in PVA/(DEX-AgNPs) and ( $12 \pm 1.7^a$ ) in DEX-PVA. Table 2 presents the antibacterial activities of DEX-PVA, DEX-AgNPs, and PVA/(DEX-AgNPs), with values presented as mean  $\pm$  standard deviation (SD) ( $n = 3$ ). Different letters (a, b, c, d, e) indicate significant differences at  $\alpha = 0.01$  and  $p < 0.05$ , as indicated by Tukey's HSD. The means differed significantly,  $F(5,12) = 48.670$ ,  $p < 0.001$ ,  $\eta^2 = 0.95$ , demonstrating a substantial effect. PVA/(DEX-AgNPs) resulted in significantly different mean depression scores.

**Table 2.** Antibacterial activity of DEX-PVA, DEX-AgNP, and PVA/(DEX-AgNPs).

Pathogen	Drug	Zone of Inhibition (Mean $\pm$ SD)
<i>Staphylococcus aureus</i>	DEX-PVA	$15.66 \pm 0.57^a$
	DEX-PVA Flim	$12 \pm 1.7^a$
	DEX-AgNPs	$20.66 \pm 2.3^b$
	DEX-AgNPs Flim	$15 \pm 1^a$
	PVA/(DEX-AgNPs)	$24.33 \pm 2.0^{b,c}$
	PVA/(DEX-AgNPs) Flim	$28.33 \pm 0.5^c$

Values are presented as means  $\pm$  SD ( $n = 3$ ). For each result, values followed by different letters (a, b, c, d, e) are significantly different at  $p < 0.05$ .

### 3.10. Molecular docking and inhibition constant analysis.

Molecular docking studies were performed using PyRx v0.8 to investigate the biological interactions between dextran and selected functional targets of *Staphylococcus aureus*, as identified based on their roles outlined in Table 3. The binding of Dextran with Staphyloferrin A and B yielded binding energies during the docking images and scores, as shown in Figure 8 (a) and (b) and Table 4. Nine docking poses were generated, indicating a high affinity for the dextran-specific binding sites in each protein. Interaction analysis demonstrated that dextran interacted with residues ARG104 and ARG60 of Staphyloferrin A and B through metal chelation. Among the 20 amino acids, leucine and tryptophan exhibited the highest binding energies to dextran. This study revealed that dextran interacts with specific amino acid residues (arginine and serine) in staphyloferrin A and B. The search algorithm analyzed and generated ligand positions at the binding sites, considering intermolecular energy, van der Waals interaction energy, hydrogen bond energy, dissolution energy, electrostatic energy, and various ligand degrees of freedom. Despite dextran showing binding affinities of -9.2 and -7.5 kcal/mol with Staphyloferrin A and B, respectively, the molecular docking analysis revealed effective interactions between dextran and Staphyloferrin A and B, resulting in reduced activity. Dextran was used to inhibit Staphyloferrin A and B enzymes at minimum

concentrations of 0.177 and 3.13  $\mu\text{mol}$ , respectively, demonstrating its strong inhibition of the *S. aureus* pathogen. This was confirmed by both in vitro and in silico analyses, which demonstrated a strong antibacterial activity.

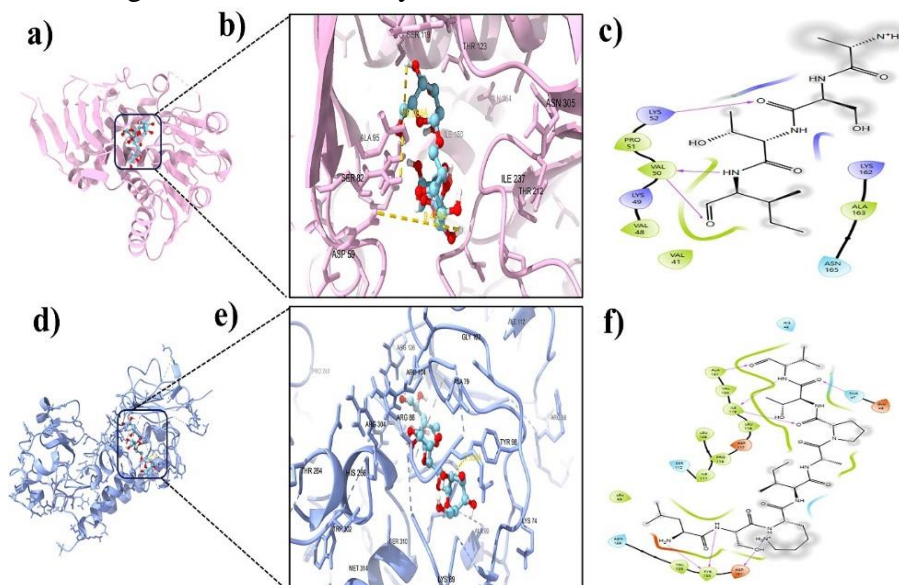


**Figure 8.** Molecular docking and interaction between dextran and the amino acid residues of (a) Stephyloferrin A; (b) Stephyloferrin B. (The left side illustrates the binding of dextran with the protein, while the right side displays the interactions between the amino acid residues and dextran, and also the 2D structure of the amino acid residues is mentioned in the figures.

**Table 3.** Molecular targets of Dextran in *Staphylococcus aureus*: structural and functional insights.

Pub Chem ID and Name	Target name	Role of Target
Dextran (4125253)	Solution structure of sortase A from <i>S. aureus</i> in complex with benzo[d] isothiazol-3-one-based inhibitor	Sortase A is a membrane-anchored cysteine transpeptidase in <i>S. aureus</i> that anchors virulence-related surface proteins to the bacterial cell wall.
	Crystal structure of SbnC in the biosynthesis of staphyloferrin B	Staphyloferrin B helps the bacteria scavenge iron from the host — essential for survival and virulence.
	Open Conformation of HtsA Complexed with Staphyloferrin A	HtsA is a lipoprotein receptor component of the HtsABC ATP-binding cassette (ABC) transporter in <i>Staphylococcus aureus</i> . It is responsible for binding and importing staphyloferrin A (SA), a citrate-based siderophore that helps the bacterium scavenge iron under nutrient-limited conditions.
	The structure of the staphyloferrin B precursor biosynthetic enzyme SbnB bound to N-(1-amino-1-carboxyl-2-ethyl)-glutamic acid and NADH	The structure of SbnB bound to ACEGA and NADH provides mechanistic insight into staphyloferrin B biosynthesis, highlighting its dual catalytic roles in precursor formation.
	Crystal structure of <i>Staphylococcus aureus</i> SirA complexed with staphyloferrin B	SirA is the substrate-binding lipoprotein component of the SirABC ABC transporter system in <i>Staphylococcus aureus</i> . It plays a critical role in iron acquisition by binding staphyloferrin B (SB), a citrate-based siderophore. SirA captures ferric-staphyloferrin B (Fe-SB) in the extracellular environment and delivers it to the SirBC transporter for internalization.

**Table 4.** Binding affinity and interaction profile of dextran with selected *Staphylococcus aurei* target.

Pub Chem ID and Name	Target name	PDB ID	Binding affinity kCal/mol	Inhibition constant $\mu\text{mol}$	Binding Sites
Dextran (4125253)	Solution structure of sortase A from <i>S. aureus</i> in complex with benzo[d] isothiazol-3-one-based inhibitor	2mlm	-6.4	20.1	Glu A:47, Asn A:56, Ser A:58, Val A: 103, Val A:108, Val A: 110, Leu A:111, Asp A:112, Gln A:113, Gln A:114, Lys A:117, Gln A: 120, Thr A: 122, Ile A:124, Arg A:139, Ile A: 141, Val A: 143

Pub Chem ID and Name	Target name	PDB ID	Binding affinity kCal/mol	Inhibition constant $\mu\text{mol}$	Binding Sites
	Crystal structure of SbnC in the biosynthesis of staphyloferrin B	7cbb	-8.2	0.96	Ser A: 143, Asp A:146, Arg A: 147, Lys A: 156, Ile A: 159, Tyr A: 167, Gln A: 44r168, Ala A: 169, Ser A: 262, Ser A: 264, Ser A: 265, Arg A: 267, Lys A: 280, Phe A: 283, Ser A: 287, Leu A: 288, Arg A: 292, Thr A: 294, Gln A: 426, Glu A: 422, Asp A: 444, Asp A: 446, Thr A: 447,
	Open Conformation of HtsA Complexed with Staphyloferrin A	3lhs	-9.2	0.177	Val A: 59, Leu A: 60, Ser A: 63, Phe A: 64, Ala A: 65, Ile A: 78, Ala A: 79, Asp A: 80, Lys A: 84, Lys A: 85, Arg A: 86, Ile A: 88, Lys A: 89, Val A: 91, Glu A:93, Ile A: 95, Tyr A: 98, Arg A: 104,, Asp A: 123, Arg A: 126 His A: 127, Ser A: 145, Phe A: 146, Arg A: 304, Ser A: 305, Arg A: 306,
	The structure of the staphyloferrin B precursor biosynthetic enzyme SbnB bound to N-(1-amino-1-carboxyl-2-ethyl)-glutamic acid and NADH	4m54	-7.5	3.13	Ile A: 57, Ala A: 58, Lys A: 78, Ile A: 80, Arg A: 94, Ala A: 95, Arg A: 60, Ser A: 119, Ser A: 120, Arg A: 122, Thr A: 123, Gly A: 148, Leu A: 149, Ile A: 150, Gly A: 151, Cys A: 213, Thr A: 214, Val A: 215, Thr A: 216, Ile A: 235, Ser A: 236, Ile A: 237, Met A: 238,
	Crystal structure of Staphylococcus aureus SirA complexed with staphyloferrin B	3mwf	-6.4	20.1	Gln A: 61, Trp A: 81, Val A: 124, Arg A: 125, Val A: 145, Phe A:146, Arg A: 201, His A: 204, Arg A: 206, Tyr A: 208, Tyr A: 212, Ile A: 238, Gln A: 240, Asn A:304, Leu A: 305,

Staphyloferrin A and B are vital siderophores produced by *S. aureus* that play crucial roles in sequestering ferric ions during infection. Understanding the biosynthetic pathways of these compounds is essential for developing effective antibacterial agents. Fur regulates iron-scavenging molecules under iron-limited conditions.

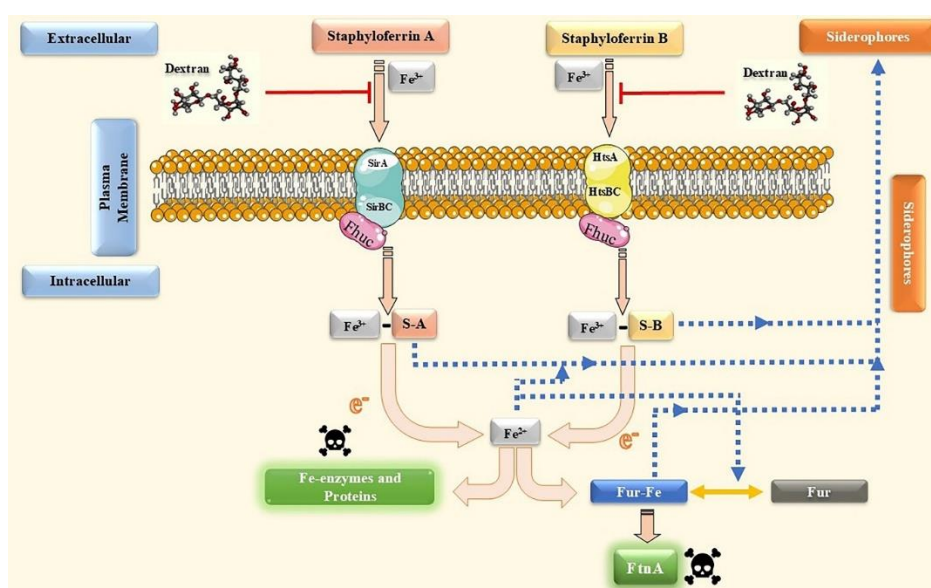


**Figure 9.** Regulation of Fe by *Staphylococcus aureus* at Iron Aquations. FtnA - ferritin gene; Fur - ferric uptake regulator; HrtAB - heme regulator transporter efflux pump; HtsABC - heme transport system involved in Fe-SA uptake; SA - Staphyloferrin A; SB - Staphyloferrin B.

FhuC acts as an ATPase that is essential for transporting staphyloferrin A and B [66]. During infection, *S. aureus* extracts iron from erythrocyte heme using enzymes, such as staphyloferrin A and B. Iron plays a key role in regulating the expression of ferritin (FtnA) in *S. aureus*. Elevated iron levels induce FtnA transcription, and the presence of iron can lead to increased ferritin expression in the liver. This regulation occurred at the transcriptional level, highlighting the significant role of iron in regulating FtnA expression. Thus, iron is crucial for the proper functioning of FtnA and for its involvement in iron storage and homeostasis in bacterial cells. Staphyloferrin A and B capture iron and transport it into the *S. aureus* cytoplasm, where it is reduced to the ferrous form, supporting protein and enzyme synthesis and promoting increased bacterial colonization [67,68]. Dextran neutralizes Staphyloferrin A and B during iron acquisition (Figure 9).

#### 4. Conclusions

In this study, silver nanoparticles (AgNPs) were successfully synthesized using dextran, DEX-PVA, and PVA/(DEX-AgNPs), and comprehensively characterized to confirm their spherical morphology, uniform dispersion, and nanoscale dimensions. FTIR analysis revealed the presence of key functional groups, including alkanes, sulfates, aromatics, and alcohols, within the biosynthesized materials, highlighting the chemical complexity and stability of hydrogel systems. Importantly, these nanocomposites exhibited potent antibacterial activity, particularly against *Staphylococcus aureus*, and effectively disrupted bacterial growth by inhibiting iron acquisition systems, specifically staphyloferrin A and B enzymes, which are essential for *S. aureus* survival under iron-limited conditions. The hydrogel films derived from these materials not only enhanced antimicrobial efficacy but also acted synergistically to inhibit key virulence pathways. Molecular docking analysis further corroborated these findings, demonstrating that dextran-associated AgNPs form stable interactions with the active sites of Staphyloferrin A and B, potentially blocking their function and thereby suppressing iron uptake and bacterial colonization. Taken together, the synthesized DEX-PVA, DEX-AgNPs, and PVA/(DEX-AgNPs) hydrogels present a promising nanomedicine platform with significant therapeutic potential for combating *S. aureus* infections, especially in clinical settings where antibiotic resistance is a growing concern.

#### Author Contributions

Conceptualization, K.J.; methodology, K.J.; writing—original draft preparation, K.J.; project administration, S.V.; resources, S.V.; supervision, S.V.; software, A.N.; validation, A.N. and E.S.; writing—review and editing, A.N. and E.S. All authors have read and agreed to the published version of the manuscript.

#### Institutional Review Board Statement

Not applicable.

#### Informed Consent Statement

Not applicable.

## Data Availability Statement

Data supporting the findings of this study are available upon reasonable request from the corresponding author.

## Funding

This research received no specific grants from any funding agency in the public, commercial, or not-for-profit sector.

## Acknowledgments

We are grateful to the Sophisticated Test and Instrumentation Center, Kochin University, Kerala, India, and the Department of Science and Technology (DST), India, for XRD and TEM analyses. In addition, we acknowledge the Chemistry and Nanoscience departments of NIT-Calicut for their support with XRD and SEM analyses.

## Conflicts of Interest

The authors declare that they have no conflicts of interest.

## References

1. Dodda, J.M.; Deshmukh, K.; Bezuidenhout, D.; Yeh, Y.-C. Hydrogels: Definition, History, Classifications, Formation, Constitutive Characteristics, and Applications. In *Multicomponent Hydrogels: Smart Materials for Biomedical Applications*, Dodda, J.M., Deshmukh, K., Bezuidenhout, D., Eds.; The Royal Society of Chemistry: **2023**; pp. 1–25, <https://doi.org/10.1039/BK9781837670055-00001>.
2. Mehta, P.; Sharma, M.; Devi, M. Hydrogels: An overview of its classifications, properties, and applications. *J. Mech. Behav. Biomed. Mater.* **2023**, *147*, 106145, <https://doi.org/10.1016/j.jmbbm.2023.106145>.
3. Ho, T.-C.; Chang, C.-C.; Chan, H.-P.; Chung, T.-W.; Shu, C.-W.; Chuang, K.-P.; Duh, T.-H.; Yang, M.-H.; Tyan, Y.-C. Hydrogels: Properties and Applications in Biomedicine. *Molecules* **2022**, *27*, 2902, <https://doi.org/10.3390/molecules27092902>.
4. Sun, G.; Mao, J.J.; Engineering Dextran-Based Scaffolds for Drug Delivery and Tissue Repair. *Nanomedicine* **2012**, *7*, 1771–1784, <https://doi.org/10.2217/nnm.12.149>.
5. Zhao, L.; Zhou, Y.; Zhang, J.; Liang, H.; Chen, X.; Tan, H. Natural Polymer-Based Hydrogels: From Polymer to Biomedical Applications. *Pharmaceutics* **2023**, *15*, 2514, <https://doi.org/10.3390/pharmaceutics15102514>.
6. Cao, H.; Duan, L.; Zhang, Y.; Cao, J.; Zhang, K. Current hydrogel advances in physicochemical and biological response-driven biomedical application diversity. *Sig. Transduct. Target. Ther.* **2021**, *6*, 426, <https://doi.org/10.1038/s41392-021-00830-x>.
7. Yang, J.; Chen, Y.; Zhao, L.; Zhang, J.; Luo, H. Constructions and Properties of Physically Cross-Linked Hydrogels Based on Natural Polymers. *Polym. Rev.* **2023**, *63*, 574-612, <https://doi.org/10.1080/15583724.2022.2137525>.
8. Patel, J.; Kumar, G.S.; Roy, H.; Maddiboyina, B.; Leporatti, S.; Bohara, R.A. From nature to nanomedicine: bioengineered metallic nanoparticles bridge the gap for medical applications. *Discover Nano* **2024**, *19*, 85, <https://doi.org/10.1186/s11671-024-04021-9>.
9. Adelnia, H.; Ensandoost, R.; Shebbrin Moonshi, S.; Gavvani, J.N.; Vasafi, E.I.; Ta, H.T. Freeze/thawed polyvinyl alcohol hydrogels: Present, past and future. *Eur. Polym. J.* **2022**, *164*, 110974, <https://doi.org/10.1016/j.eurpolymj.2021.110974>.
10. Li, S.; Wang, N.; Yu, B.; Sun, W.; Wang, L.; Genetically encoded chemical crosslinking of carbohydrate. *Nat. Chem.* **2023**, *15*, 33–42, <https://doi.org/10.1038/s41557-022-01059-z>.
11. Petrovici, A.R.; Pinteala, M.; Simionescu, N. Dextran Formulations as Effective Delivery Systems of Therapeutic Agents. *Molecules* **2023**, *28*, 1086, <https://doi.org/10.3390/molecules28031086>.

12. Joshi, N.; Pandey, D.K.; Mistry, B.G.; Singh, D.K. Metal Oxide Nanoparticles: Synthesis, Properties, Characterization, and Applications. In *Nanomaterials: Advances and Applications*, Singh, D.K., Singh, S., Singh, P., Eds.; Springer Nature Singapore: Singapore, **2023**; pp. 103-144, [https://doi.org/10.1007/978-981-19-7963-7\\_5](https://doi.org/10.1007/978-981-19-7963-7_5).
13. Natsuki, J.; Natsuki, T.; Hashimoto, Y. A review of silver nanoparticles: synthesis methods, properties and applications. *Int. J. Mater. Sci. Appl* **2015**, *4*, 325-332, <https://doi.org/10.11648/j.ijmsa.20150405.17>.
14. Nene, A.; Galluzzi, M.; Hongrong, L.; Somani, P.; Ramakrishna, S.; Yu, X.-F. Synthetic preparations and atomic scale engineering of silver nanoparticles for biomedical applications. *Nanoscale* **2021**, *13*, 13923-13942, <https://doi.org/10.1039/D1NR01851E>.
15. Abbas, R.; Luo, J.; Qi, X.; Naz, A.; Khan, I.A.; Liu, H.; Yu, S.; Wei, J. Silver Nanoparticles: Synthesis, Structure, Properties and Applications. *Nanomaterials* **2024**, *14*, 1425, <https://doi.org/10.3390/nano14171425>.
16. Liu, H.; Zhong, L.; Yun, K.; Samal, M. Synthesis, characterization, and antibacterial properties of silver nanoparticles-graphene and graphene oxide composites. *Biotechnol. Bioprocess Eng.* **2016**, *21*, 1-18, <https://doi.org/10.1007/s12257-015-0733-5>.
17. Altammar, K.A. A review on nanoparticles: characteristics, synthesis, applications, and challenges. *Front. Microbiol.* **2023**, *14*, 1155622, <https://doi.org/10.3389/fmicb.2023.1155622>.
18. Anees Ahmad, S.; Sachi Das, S.; Khatoon, A.; Tahir Ansari, M.; Afzal, M.; Saquib Hasnain, M.; Kumar Nayak, A. Bactericidal activity of silver nanoparticles: A mechanistic review. *Mater. Sci. Energy Technol.* **2020**, *3*, 756-769, <https://doi.org/10.1016/j.mset.2020.09.002>.
19. Pal, N.; Agarwal, M.; Ghosh, A. Green synthesis of silver nanoparticles using polysaccharide-based guar gum. *Mater. Today Proc.* **2023**, *76*, 212-218, <https://doi.org/10.1016/j.matpr.2023.01.048>.
20. Sharma, N.K. Chapter 12 - Structural and functional role of cellulases. In *Current Status and Future Scope of Microbial Cellulases*, Tuli, D.K., Kuila, A., Eds.; Elsevier: **2021**; pp. 255-273, <https://doi.org/10.1016/B978-0-12-821882-2.00013-2>.
21. Azeera, M.; Vaidevi, S.; Ruckmani, K. Characterization Techniques of Hydrogel and Its Applications. In *Cellulose-Based Superabsorbent Hydrogels*, Mondal, M.I.H., Ed.; Springer International Publishing: Cham, **2019**; pp. 737-761, [https://doi.org/10.1007/978-3-319-77830-3\\_25](https://doi.org/10.1007/978-3-319-77830-3_25).
22. Kamoun, E.A.; Kenawy, E.-R.S.; Chen, X. A review on polymeric hydrogel membranes for wound dressing applications: PVA-based hydrogel dressings. *J. Adv. Res.* **2017**, *8*, 217-233, <https://doi.org/10.1016/j.jare.2017.01.005>.
23. Bashir, S.; Hina, M.; Iqbal, J.; Rajpar, A.H.; Mujtaba, M.A.; Alghamdi, N.A.; Wageh, S.; Ramesh, K.; Ramesh, S. Fundamental Concepts of Hydrogels: Synthesis, Properties, and Their Applications. *Polymers* **2020**, *12*, 2702, <https://doi.org/10.3390/polym12112702>.
24. Giri, A.K.; Jena, B.; Biswal, B.; Pradhan, A.K.; Arakha, M.; Acharya, S.; Acharya, L. Green synthesis and characterization of silver nanoparticles using *Eugenia roxburghii* DC. extract and activity against biofilm-producing bacteria. *Sci. Rep.* **2022**, *12*, 8383, <https://doi.org/10.1038/s41598-022-12484-y>.
25. Kanimozhi, J.; Moorthy, I.G.; Sivashankar, R.; Sivasubramanian, V. Optimization of dextran production by *Weissella cibaria* NITCSK4 using Response Surface Methodology-Genetic Algorithm based technology. *Carbohydr. Polym.* **2017**, *174*, 103-110, <https://doi.org/10.1016/j.carbpol.2017.06.021>.
26. Bankura, K.P.; Maity, D.; Mollick, M.M.R.; Mondal, D.; Bhowmick, B.; Bain, M.K.; Chakraborty, A.; Sarkar, J.; Acharya, K.; Chattopadhyay, D. Synthesis, characterization and antimicrobial activity of dextran stabilized silver nanoparticles in aqueous medium. *Carbohydr. Polym.* **2012**, *89*, 1159-1165, <https://doi.org/10.1016/j.carbpol.2012.03.089>.
27. Luthfianti, H.R.; Waresindo, W.X.; Edikresnha, D.; Chahyadi, A.; Suciati, T.; Noor, F.A.; Khairurrijal, K. Physicochemical Characteristics and Antibacterial Activities of Freeze-Thawed Polyvinyl Alcohol/Andrographolide Hydrogels. *ACS Omega* **2023**, *8*, 2915-2930, <https://doi.org/10.1021/acsomega.2c05110>.
28. Sharifi-Rad, M.; Elshafie, H.S.; Pohl, P. Green synthesis of silver nanoparticles (AgNPs) by *Lallemantia royleana* leaf Extract: Their Bio-Pharmaceutical and catalytic properties. *J. Photochem. Photobiol. A: Chem.* **2024**, *448*, 115318, <https://doi.org/10.1016/j.jphotochem.2023.115318>.
29. Zhang, K.; Feng, W.; Jin, C. Protocol efficiently measuring the swelling rate of hydrogels. *MethodsX* **2020**, *7*, 100779, <https://doi.org/10.1016/j.mex.2019.100779>.
30. Bano, N.; Iqbal, D.; Al Othaim, A.; Kamal, M.; Albadrani, H.M.; Algehainy, N.A.; Alyenbaawi, H.; Alghofaili, F.; Amir, M.; Roohi. Antibacterial efficacy of synthesized silver nanoparticles of *Microbacterium*

- proteolyticum* LA2(R) and *Streptomyces rochei* LA2(O) against biofilm forming meningitis causing microbes. *Sci. Rep.* **2023**, *13*, 4150, <https://doi.org/10.1038/s41598-023-30215-9>.
31. Urnukhsaikhan, E.; Bold, B.-E.; Gunbileg, A.; Sukhbaatar, N.; Mishig-Ochir, T. Antibacterial activity and characteristics of silver nanoparticles biosynthesized from *Carduus crispus*. *Sci. Rep.* **2021**, *11*, 21047, <https://doi.org/10.1038/s41598-021-00520-2>.
  32. Agu, P.C.; Afiukwa, C.A.; Orji, O.U.; Ezech, E.M.; Ofoke, I.H.; Ogbu, C.O.; Ugwuja, E.I.; Aja, P.M. Molecular docking as a tool for the discovery of molecular targets of nutraceuticals in diseases management. *Sci. Rep.* **2023**, *13*, 13398, <https://doi.org/10.1038/s41598-023-40160-2>.
  33. Darras, F.H.; Pang, Y.-P. On the use of the experimentally determined enzyme inhibition constant as a measure of absolute binding affinity. *Biochem. Biophys. Res. Commun.* **2017**, *489*, 451–454, <https://doi.org/10.1016/j.bbrc.2017.05.168>.
  34. Sharma, V.K.; Yngard, R.A.; Lin, Y. Silver nanoparticles: Green synthesis and their antimicrobial activities. *Adv. Colloid Interface Sci.* **2009**, *145*, 83–96, <https://doi.org/10.1016/j.cis.2008.09.002>.
  35. Paramelle, D.; Sadovoy, A.; Gorelik, S.; Free, P.; Hobley, J.; Fernig, D.G. A rapid method to estimate the concentration of citrate capped silver nanoparticles from UV-visible light spectra. *Analyst* **2014**, *139*, 4855–4861, <https://doi.org/10.1039/C4AN00978A>.
  36. Irvani, S. Green synthesis of metal nanoparticles using plants. *Green Chem.* **2011**, *13*, 2638–2650, <https://doi.org/10.1039/c1gc15386b>.
  37. Korbog, I.; Mohamed Saleh, S. Studies on the formation of intermolecular interactions and structural characterization of polyvinyl alcohol/lignin film. *Int. J. Environ. Stud.* **2016**, *73*, 226–235, <https://doi.org/10.1080/00207233.2016.1143700>.
  38. Hajji, S.; Chaker, A.; Jridi, M.; Maalej, H.; Jellouli, K.; Boufi, S.; Nasri, M. Structural analysis, and antioxidant and antibacterial properties of chitosan-poly (vinyl alcohol) biodegradable films. *Environ. Sci. Pollut. Res.* **2016**, *23*, 15310–15320, <https://doi.org/10.1007/s11356-016-6699-9>.
  39. Nguyen, L.H.; Tran, T.T.; Nguyen, T.-M.T.; Le, H.V.; Nguyen, K.-P.L.; Vu, A.N. Fabrication of a ternary biocomposite film based on polyvinyl alcohol, cellulose nanocrystals, and silver nanoparticles for food packaging. *RSC Adv.* **2024**, *14*, 18671–18684, <https://doi.org/10.1039/D4RA02085E>.
  40. Loo, C.-Y.; Young, P.M.; Lee, W.-H.; Cavaliere, R.; Whitchurch, C.B.; Rohanizadeh, R. Non-cytotoxic silver nanoparticle-polyvinyl alcohol hydrogels with anti-biofilm activity: designed as coatings for endotracheal tube materials. *Biofouling* **2014**, *30*, 773–788, <https://doi.org/10.1080/08927014.2014.926475>.
  41. Mahanta, N.; Valiyaveetil, S. *In situ* preparation of silver nanoparticles on biocompatible methacrylated poly(vinyl alcohol) and cellulose based polymeric nanofibers. *RSC Adv.* **2012**, *2*, 11389–11396, <https://doi.org/10.1039/c2ra20637d>.
  42. Madkhali, O.A.; Sivagurunathan Moni, S.; Sultan, M.H.; Bukhary, H.A.; Ghazwani, M.; Alhakamy, N.A.; Meraya, A.M.; Alshahrani, S.; Alqahtani, S.S.; Bakkari, M.A.; Alam, M.I.; Elmobark, M.E. Formulation and evaluation of injectable dextran sulfate sodium nanoparticles as a potent antibacterial agent. *Sci. Rep.* **2021**, *11*, 9914, <https://doi.org/10.1038/s41598-021-89330-0>.
  43. Can, H.K.; Kavlak, S.; ParviziKhosroshahi, S.; Güner, A. Preparation, characterization and dynamical mechanical properties of dextran-coated iron oxide nanoparticles (DIONPs). *Artif. Cells Nanomed. Biotechnol.* **2018**, *46*, 421–431, <https://doi.org/10.1080/21691401.2017.1315428>.
  44. Ahmed, E.M. Hydrogel: Preparation, characterization, and applications: A review. *J. Adv. Res.* **2015**, *6*, 105–121, <https://doi.org/10.1016/j.jare.2013.07.006>.
  45. Rzayev, Z.M.O.; Türk, M.; Uzgören, A. Bioengineering functional copolymers. XV. Synthesis and characterization of poly(*N*-isopropyl acrylamide-*co*-3,4-dihydro-2H-pyran-*alt*-maleic anhydride)s and their PEO branched derivatives. *J. Polym. Sci. A Polym. Chem.* **2010**, *48*, 4285–4295, <https://doi.org/10.1002/pola.24217>.
  46. Peppas, N.A.; Hilt, J.Z.; Khademhosseini, A.; Langer, R. Hydrogels in Biology and Medicine: From Molecular Principles to Bionanotechnology. *Adv. Mater.* **2006**, *18*, 1345–1360, <https://doi.org/10.1002/adma.200501612>.
  47. Zhang, M.; Jiang, S.; Han, F.; Li, M.; Wang, N.; Liu, L. Anisotropic cellulose nanofiber/chitosan aerogel with thermal management and oil absorption properties. *Carbohydr. Polym.* **2021**, *264*, 118033, <https://doi.org/10.1016/j.carbpol.2021.118033>.
  48. Li, N.; Zhu, Z.; Dong, Q.; Li, J.; Yang, Z.; Chueh, C.-C.; Jen, A.K.Y.; Wang, L. Enhanced Moisture Stability of Cesium-Containing Compositional Perovskites by a Feasible Interfacial Engineering. *Adv. Mater. Interfaces* **2017**, *4*, 1700598, <https://doi.org/10.1002/admi.201700598>.

49. Battista, S.; Guarnieri, D.; Borselli, C.; Zeppetelli, S.; Borzacchiello, A.; Mayol, L.; Gerbasio, D.; Keene, D.R.; Ambrosio, L.; Netti, P.A. The effect of matrix composition of 3D constructs on embryonic stem cell differentiation. *Biomaterials* **2005**, *26*, 6194–6207, <https://doi.org/10.1016/j.biomaterials.2005.04.003>.
50. Zou, Y.; Liu, X. Morphology, thermal and mechanical properties of glass fiber-reinforced crosslinkable poly(arylene ether nitrile). *J. Appl. Polym. Sci.* **2013**, *129*, 130–137, <https://doi.org/10.1002/app.38712>.
51. Singh, S.K.; Kumar, Y.; Ravindranath, S.S. Thermal degradation of SBS in bitumen during storage: Influence of temperature, SBS concentration, polymer type and base bitumen. *Polym. Degrad. Stab.* **2018**, *147*, 64–75, <https://doi.org/10.1016/j.polymdegradstab.2017.11.008>.
52. Torres, F.G.; Arroyo, J.J.; Troncoso, O.P. Bacterial cellulose nanocomposites: An all-nano type of material. *Mater. Sci. Eng. C* **2019**, *98*, 1277–1293, <https://doi.org/10.1016/j.msec.2019.01.064>.
53. Wang, X.; Tarahomi, M.; Sheibani, R.; Xia, C.; Wang, W. Progresses in lignin, cellulose, starch, chitosan, chitin, alginate, and gum/carbon nanotube (nano)composites for environmental applications: A review. *Int. J. Biol. Macromol.* **2023**, *241*, 124472, <https://doi.org/10.1016/j.ijbiomac.2023.124472>.
54. Nishiyabu, R.; Takahashi, Y.; Yabuki, T.; Gommori, S.; Yamamoto, Y.; Kitagishi, H.; Kubo, Y. Boronate sol–gel method for one-step fabrication of polyvinyl alcohol hydrogel coatings by simple cast- and dip-coating techniques. *RSC Adv.* **2020**, *10*, 86–94, <https://doi.org/10.1039/C9RA08208E>.
55. Eid, M.; El-Arnaouty, M.B.; Salah, M.; Soliman, E.-S.; Hegazy, E.-S.A. Radiation synthesis and characterization of poly(vinyl alcohol)/poly(N-vinyl-2-pyrrolidone) based hydrogels containing silver nanoparticles. *J. Polym. Res.* **2012**, *19*, 9835, <https://doi.org/10.1007/s10965-012-9835-3>.
56. Travan, A.; Pelillo, C.; Donati, I.; Marsich, E.; Benincasa, M.; Scarpa, T.; Semeraro, S.; Turco, G.; Gennaro, R.; Paoletti, S. Non-cytotoxic Silver Nanoparticle-Polysaccharide Nanocomposites with Antimicrobial Activity. *Biomacromolecules* **2009**, *10*, 1429–1435, <https://doi.org/10.1021/bm900039x>.
57. Sambalova, O.; Thorwarth, K.; Heeb, N.V.; Bleiner, D.; Zhang, Y.; Borgschulte, A.; Kroll, A. Carboxylate Functional Groups Mediate Interaction with Silver Nanoparticles in Biofilm Matrix. *ACS Omega* **2018**, *3*, 724–733, <https://doi.org/10.1021/acsomega.7b00982>.
58. Carré-Rangel, L.; Alonso-Nuñez, G.; Espinoza-Gómez, H.; Flores-López, L.Z. Green Synthesis of Silver Nanoparticles: Effect of Dextran Molecular Weight Used as Stabilizing-Reducing Agent. *J. Nanosci. Nanotechnol.* **2015**, *15*, 9849–9855, <https://doi.org/10.1166/jnn.2015.10334>.
59. Morrissey, J.A.; Cockayne, A.; Brummell, K.; Williams, P. The Staphylococcal Ferritins Are Differentially Regulated in Response to Iron and Manganese and via PerR and Fur. *Infect. Immun.* **2004**, *72*, 972–979, <https://doi.org/10.1128/IAI.72.2.972-979.2004>.
60. van Dijk, M.C.; de Kruijff, R.M.; Hagedoorn, P.-L. The Role of Iron in *Staphylococcus aureus* Infection and Human Disease: A Metal Tug of War at the Host—Microbe Interface. *Front. Cell Dev. Biol.* **2022**, *10*, 857237, <https://doi.org/10.3389/fcell.2022.857237>.
61. Hammer, N.D.; Skaar, E.P. Molecular Mechanisms of *Staphylococcus aureus* Iron Acquisition. *Annu. Rev. Microbiol.* **2011**, *65*, 129–147, <https://doi.org/10.1146/annurev-micro-090110-102851>.

## Publisher’s Note & Disclaimer

The statements, opinions, and data presented in this publication are solely those of the individual author(s) and contributor(s) and do not necessarily reflect the views of the publisher and/or the editor(s). The publisher and/or the editor(s) disclaim any responsibility for the accuracy, completeness, or reliability of the content. Neither the publisher nor the editor(s) assume any legal liability for any errors, omissions, or consequences arising from the use of the information presented in this publication. Furthermore, the publisher and/or the editor(s) disclaim any liability for any injury, damage, or loss to persons or property that may result from the use of any ideas, methods, instructions, or products mentioned in the content. Readers are encouraged to independently verify any information before relying on it, and the publisher assumes no responsibility for any consequences arising from the use of materials contained in this publication.

Supplementary materials

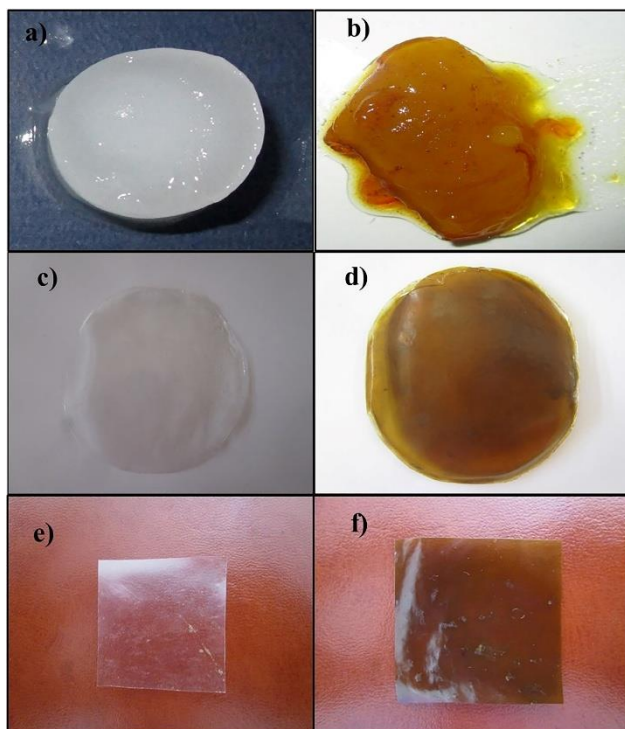


**Figure S1.** (a) The Prepared hydrogel composites of DEX-PVA, (b) hydrogel of PVA/(DEX-AgNPs), (c) dried hydrogel of DEX-PVA, (d) dried hydrogel of PVA/(DEX-AgNPs), (e) Film of dried hydrogel of DEX-PVA, (f) Film of hydrogel of PVA/(DEX-AgNPs).